The NOSL-296 high resolution 14N216O line list for atmospheric applications

S.A. Tashkun, A. Campargue

▶ **To cite this version:**

S.A. Tashkun, A. Campargue. The NOSL-296 high resolution 14N216O line list for atmospheric applications. Journal of Quantitative Spectroscopy and Radiative Transfer, 2023, 295, pp.108417. 10.1016/j.jqsrt.2022.108417 . hal-04257880

HAL Id: hal-04257880
https://hal.science/hal-04257880

Submitted on 25 Oct 2023

HAL is a multi-disciplinary open access archive for the deposit and dissemination of scientific research documents, whether they are published or not. The documents may come from teaching and research institutions in France or abroad, or from public or private research centers.

L'archive ouverte pluridisciplinaire **HAL**, est destinée au dépôt et à la diffusion de documents scientifiques de niveau recherche, publiés ou non, émanant des établissements d'enseignement et de recherche français ou étrangers, des laboratoires publics ou privés.

The NOSL-296 high resolution $^{14}N_2{}^{16}O$ line list for atmospheric applications

S.A. Tashkun [a], *A. Campargue* [b]

[a] V.E. Zuev Institute of Atmospheric Optics, 1, Academician Zuev square, 634055 Tomsk, Russia
[b] Univ. Grenoble Alpes, CNRS, LIPhy, 38000 Grenoble, France

Graphical abstract

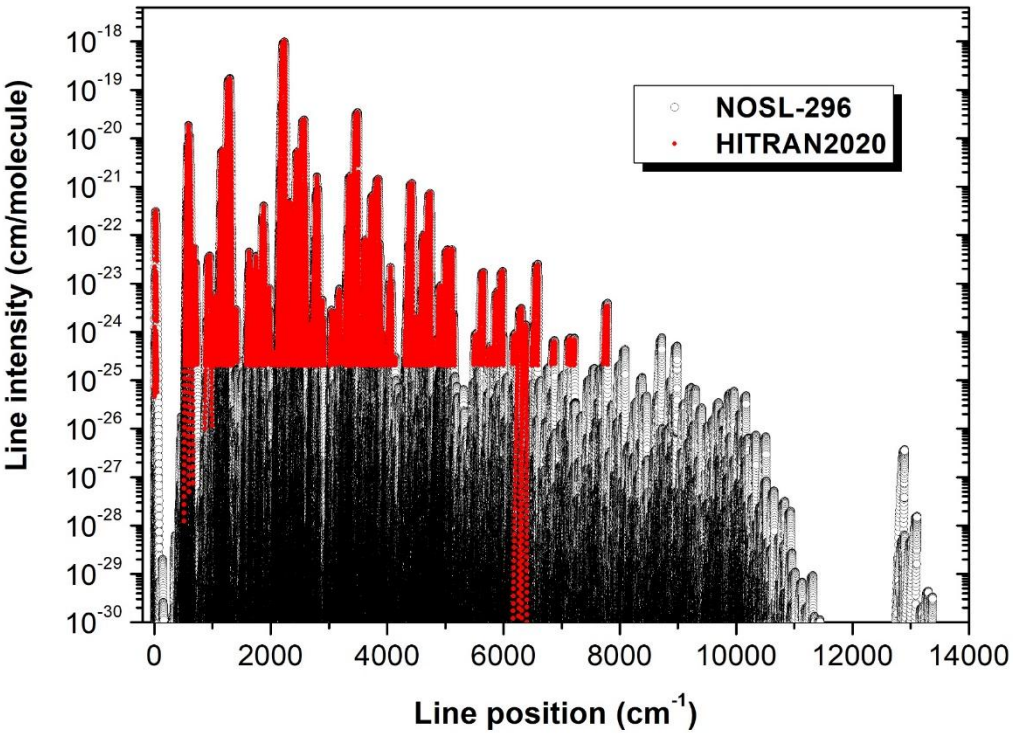

Keywords:
Nitrous oxide; N2O; line intensity; dipole moment, HITRAN

Abstract

The Nitrous Oxide Spectroscopic Line list (NOSL-296) presented in this work is an empirical line list for the main isotopologue of nitrous oxide, $^{14}N_2{}^{16}O$, mainly dedicated to atmospheric applications. It contains line positions and intensities at a reference temperature of 296 K calculated using the effective operator approach. The intensity cutoff is 10^{-30} cm/molecule. Almost 900,000 lines covering the 0.02-13,378 cm^{-1} spectral range are included in NOSL-296. The line list is based on the fitted non-polyad models of the effective Hamiltonian and effective dipole moment operator describing globally an exhaustive review of experimental data collected from the literature (more than 51500 line intensities). The non-polyad model of effective Hamiltonian has been elaborated in Tashkun SA, J Quant Spectrosc Radiat Transfer 2019;231:88-101. doi 10.1016/j.jqsrt.2019.04.023 while the non-polyad model of the effective dipole moment operator is developed in the present work. The fitted models are able to reproduce measured positions and intensities with accuracies compatible with measurement uncertainties. Comparison of NOSL-296 with HITRAN2020 and Ames-296 line lists are discussed. The NOSL-296 line list is provided as a Supplementary Material and freely accessible at https://ftp.iao.ru/pub/LTS/NOSL-296/

1. Introduction

The main goal of this work is to create a room temperature line list (NOSL-296) for the main isotopologue of nitrous oxide, $^{14}N_2{}^{16}O$. The Nitrous Oxide Spectroscopic Line list (NOSL-296) is proposed to improve the sets of line positions and line intensities in the future versions of the HITRAN [1] and GEISA [2] databanks. The sources for the $^{14}N_2{}^{16}O$ data provided in the successive versions of the HITRAN database are summarized below.

HITRAN2004 [3] line positions and intensities were taken from the SISAM.N2O line list of Toth [4]. This list covers the 500 - 7,500 cm^{-1} spectral range with a minimum line strength of 2.02×10^{-25} cm/molecule at 296 K. Most of the line positions and line intensities are calculated values obtained using spectroscopic parameters obtained from a band-by-band fit of line positions and line intensities measured by Fourier transform spectroscopy (FTS). The line positions and intensities of the 0001-1000 laser band in the 10-μm region were replaced with measurements by Daumont et al. [5]. [Here, we use the normal mode labeling of the vibrational levels, $V_1V_2l_2V_3$ where V_i= 1-3 are the vibrational quantum numbers and l_2 the vibrational angular momentum of the bending mode]. The line positions and intensities in the 0–50 cm^{-1} region were retained from HITRAN2000 [6].

HITRAN2008 [7] reproduced HITRAN2004 with minor corrections and additions. Namely, two strong *P*(1) lines (at 578.5261 and 1167.2943 cm^{-1}) were added. Also, six lines of the weak, strongly perturbed 0600–1000 band around 4.6 μm were added. The HITRAN2008 list of $^{14}N_2{}^{16}O$ were kept unchanged in the HITRAN2012 [8] and HITRAN2016 [9] versions. Finally, the intensities of the 4200-0000 and 5000-0000 bands near 1.6 μm were improved in the HITRAN2020 list [1].

Thus, most of the $^{14}N_2{}^{16}O$ HITRAN2020 line positions and intensities are, in fact, unchanged since HITRAN2004 while a huge number of measurements have become available in the two last decades. For the GEISA2020 databank [2], the situation is similar, most data originating from Toth's line list [4].

There are three other (calculated) line lists available for $^{14}N_2{}^{16}O$. The Nitrous Oxide Spectroscopy Databank (NOSD) [11] constructed using the effective operator approach extends up to 8310 cm^{-1}. The HITEMP line list [10] is a mixture of the HITRAN2016 [9] and NOSD-1000 [11] line lists. The HITEMP format is compatible with HITRAN format (the HITEMP reference temperature is 296 K). The line list contains about 3.5 million transitions. The third list is the room temperature line list, not yet published, developed by the Ames team [12]. The Ames list is based on an empirical potential energy surface (PES) and a pure *ab initio* dipole moment surface. The $^{14}N_2{}^{16}O$ Ames line list was computed under the following

conditions: natural isotopic abundance, reference temperature of 296 K, upper state energy cutoff of 20,000 cm^{-1}, line intensity cutoff at 296 K of 10^{-31} cm/molecule and frequency range from 0 to15,000 cm^{-1}. The number of entries is about 1.4 million transitions. The Ames list will be considered below for a detailed comparison with our NOSL-296 list.

The principal isotopologue of nitrous oxide, $^{14}N_2{}^{16}O$, is a non-symmetric linear triatomic molecule. Its equilibrium configuration in the ground electronic state belongs to the $C_{\infty V}$ symmetry point group. Due to the approximate relations between the harmonic frequencies $\omega_3 \approx 2\omega_1 \approx 4\omega_2$, its vibrational states can be grouped according to the polyad number

$$P = 2V_1 + V_2 + 4V_3 \quad (1.1)$$

where V_1, V_2, and V_3 are degrees of excitation of the stretch (Σ_+), bend (Π), and stretch (Σ_+) normal modes. A vibration-rotation state of $^{14}N_2{}^{16}O$ is fully characterized by six quantum numbers V_1, V_2, l_2, V_3, J, ε, where J is the total angular momentum quantum number, l_2 is the vibrational angular momentum quantum number: l_2 = -V_2, -V_2+2, ..., V_2-2, V_2, and ε is Wang symmetry, ε= 1 for e-type states and ε= 2 for f-type states. The numbers l_2 and V_2 have the same parity. This nomenclature which is adopted in the HITRAN and GEISA databases, will be used in the following.

The above-mentioned NOSD and HITEMP line lists were calculated in the frame of a global effective model assuming no couplings between states belonging to different polyads. In fact, a number of interpolyad couplings have been experimentally evidenced which obliged to develop a non-polyad model of effective Hamiltonian to account for the measured line positions [13]. In this work, we develop a non-polyad model of the Effective Dipole Moment (EDM) to compute the corresponding line intensities with accuracies compatible with measurement uncertainties. The EDM parameters of the model were fitted to the measured and SISAM [4] line intensities collected from the literature. During the fitting process, the eigenfunctions of the fitted non-polyad Effective Hamiltonian (EH) model [13] were used. The model has spectroscopic level of accuracy: the root-mean-square of the (meas. –calc.) deviations is 0.006 cm^{-1} [13]. The fitted EDM model presented below is able to reproduce more than 27,000 measured and near 25,000 SISAM.N2O rotation-vibration line intensities of $^{14}N_2{}^{16}O$ with accuracies compatible with measurement uncertainties. The resulting NOSL-296 line list covers the 0.02 - 13,378 spectral range and counts 889,508 transitions with intensities above an intensity cutoff of 10^{-30} cm/molecule.

The paper is organized as follows. The non-polyad EDM model is presented in the next Section 2. The input data file of the measured and calculated line intensities is described in

Section 3. In Section 4, we describe the algorithm and results of the fitting of the model parameters to the input data. In Section 5, the obtained NOSL-296 line list is presented before the discussion of the comparison with Ames-296 and HITRAN2020 lists (Section 6). Finally, a summary of the results obtained is presented together with a discussion of the best recommended line list (Section 7).

2. Non-polyad effective dipole moment model

The line intensity, $S_{i\to f}(T)$, of a vibrational-rotational transition from the initial *i* to final *f* states is given by the well-known equation:

$$S_{i\to f}(T) = \frac{8\pi^3}{3hc} C\sigma_{i\to f} \frac{\exp(1-hcE_i/kT)}{Q(T)} \left[1 - \exp\left(-hc\sigma_{i\to f}/kT\right)\right] W_{i\to f}, \qquad (2.1)$$

where *T* is the temperature, *h* is the Planck constant, *c* is speed of the light, *C* is the isotopic abundance, $\sigma_{i\to f}$ is the transition frequency, E_i is the energy of the lower state, *k* is the Boltzmann constant. *Q(T)* is the partition function and $W_{i\to f}$ is the line strength. Within the effective operator approach applied to a linear triatomic molecule, the line strength is given by the equation

$$W_{i\to f} = |<\Psi_f^{eff}|\mu_Z^{eff}|\Psi_i^{eff}>|^2, \qquad (2.2)$$

where Ψ_i^{eff}, E_i and Ψ_f^{eff}, E_f are the eigenfunctions and eigenvalues of the effective Hamiltonian H^{eff} of the initial and final states, respectively:

$$H^{eff}\Psi_i^{eff} = E_i\Psi_i^{eff} \text{ and } H^{eff}\Psi_f^{eff} = E_f\Psi_f^{eff}. \qquad (2.3)$$

μ_Z^{eff} is the EDM operator which is obtained from the space-fixed component μ_z by the same contact transformations as the EH from a vibration-rotation molecular Hamiltonian. Symbols *i* and *f* stand for composite sets of quantum numbers specifying initial and final vibration-rotation states of the transitions.

The matrices of EH are constructed in Wang-type basis defined as

$$|V_1, V_2, |l_2|, V_3, J, C>= \frac{1}{\sqrt{2}}(|V_1, V_2, l_2, V_3, J> + (-1)^{C-1}|V_1, V_2, -l_2, V_3, J>)$$

$$|V_1, V_2, 0, V_3, J, 1>= |V_1, V_2, 0, V_3, J>, \qquad (2.4)$$

with *C*= 1 (*e*-parity basis functions) and *C*= 2 (*f*-parity basis functions). The complete expression of the non-polyad EH matrix elements in this basis are given in [13].

The basis functions are ordered in increasing order of the polyad number *P*. Since *J* and *C* are good quantum numbers, the EH matrix in this basis, H^{eff}, is bock-diagonal with respect

to J and C and thus each H_{JC}^{eff} matrix can be diagonalized independently. The eigenproblem (2.3) for the non-polyad EH model can be written as:

$$H_{JCN}^{eff}\Psi_{JCN}^{eff} = E_{JCN}\Psi_{JCN}^{eff}, \tag{2.5}$$

where N = 1, 2, …. is the ranking index numbering the eigenvalues of the H_{JC}^{eff} matrix in ascending order. Since the polyads overlap due to interpolyad interactions, the H_{JC}^{eff} matrix has infinite size and thus must be truncated for computing. It is done by fixing the maximum polyad number, P_{max}. The H_{JC}^{eff} matrix includes all basis functions which belong to the polyads 0, 1, …, $P_{max.}$

In the frame of the polyad EH model, each H_{JC}^{eff} matrix is block-diagonal with respect to the polyad number, P. Each H_{JCP}^{eff} block for P = 0, 1, …, P_{max} can be diagonalized separately:

$$H_{JCPn}^{eff}\Psi_{JCPn}^{eff} = E_{JCPn}\Psi_{JCPn}^{eff}, \tag{2.6}$$

Where the index n = 1, 2, …. is the ranking index numbering the eigenvalues of the H_{JCP}^{eff} matrix in increasing order. Within the polyad model, the eigenfunctions are

$$\Psi_{JCPn}^{eff} = \sum_{V_1,V_2,l_2,V_3\in P} T_{V_1,V_2,l_2,V_3}^{JCP}|V_1,V_2,|l_2|,V_3,J,C>, \tag{2.7}$$

where $T_{V_1,V_2,|l_2|,V_3}^{JCP}$ are the mixing coefficients which define the contributions of the basis functions $|V_1,V_2,|l_2|,V_3,J,C>$ of the polyad P in an eigenfunction.

For a non-polyad EH model, the expansion of an eigenfunction reads

$$\Psi_{JCN}^{eff} = \sum_{P=0}^{P_{max}} \sum_{V_1,V_2,l_2,V_3\in P} T_{V_1,V_2,l_2,V_3}^{JC}|V_1,V_2,|l_2|,V_3,J,C>. \tag{2.8}$$

which leads to the matrix element of the EDM for operator:

$$\begin{aligned} &<\Psi_f^{eff}|\mu_Z^{eff}|\Psi_i^{eff}>= \\ &\sum_{P\prime=0}^{P\prime max}\sum_{P"=0}^{P"max} \sum_{V_1',V_2',l_2',V_3'\in P\prime} \sum_{V_1'',V_2'',l_2'',V_3''\in P"} T_{V_1',V_2',l_2',V_3'}^{J_f,C_f} T_{V_1'',V_2'',l_2'',V_3''}^{J_i,C_i} \times \\ &<V_1',V_2',|l_2'|,V_3',J_f,C_f|\mu_Z^{eff}|V_1'',V_2'',|l_2''|,V_3'',J_i,C_i>, \end{aligned} \tag{2.9}$$

where prime and double prime denote the final state f and initial state i, respectively.

The matrix elements of the non-polyad EDM operator are closely related to those developed for the polyad EDM operator [14-16]:

$$<V_1', V_2', |l_2'|, V_3', J_f, C_f|\mu_Z^{eff}|V_1'', V_2'', |l_2''|, V_3'', J_i, C_i>=$$

$$\sqrt{\Gamma(V', l_2', \Delta V, \Delta l_2)\left(1+\delta_{l_2'}+\delta_{l_2''}-2\delta_{l_2'}\delta_{l_2''}\right)}\Phi(\Delta J, \Delta l_2)\times \left[M_{\Delta V}^{|\Delta l_2|}+\kappa_{\Delta V,1}^{|\Delta l_2|}V_1+\kappa_{\Delta V,2}^{|\Delta l_2|}V_2+\kappa_{\Delta V,3}^{|\Delta l_2|}V_3+F(J, l_2, \Delta V, \Delta l_2)\right], \quad (2.10)$$

where

$V' = (V_1', V_2', V_3'), \Delta V = (V_1' - V_1'', V_2' - V_2'', V_3' - V_3''), \Delta l_2 = l_2' - l_2'', J = J_f, \Delta J = J_f - J_i.$

The function $\Gamma(V, l_2, \Delta V, \Delta l_2)$ is tabulated in Table 1 of Ref. [14] for small values of ΔV. The factor with the combination of Kronecker symbols appears inside the square root in Eq. (2.10) because we use Wang-type basis functions.

The function $\Phi(\Delta J, \Delta l_2)$ [16] for Δl_2 = 0, ±1 is equal to the Clebsch-Gordan coefficient

$$\Phi(J, l_2, \Delta J, \Delta l_2) = (1, \Delta l_2, J, l_2|J+\Delta J, l_2+\Delta l_2)$$

and for Δl_2 = ±2 it can be written as

$$\Phi(J, l_2, 1, \pm 2) = (1, \pm 1, J, l_2|J+1, l_2 \pm 1)\sqrt{(J \mp l_2)(J \pm l_2 + 3)}$$

$$\Phi(J, l_2, 0, \pm 2) = (1, \pm 1, J, l_2|J, l_2 \pm 1)\sqrt{(J \mp l_2 - 1)(J \pm l_2 + 2)}$$

$$\Phi(J, l_2, -1, \pm 2) = (1, \pm 1, J, l_2|J-1, l_2 \pm 1)\sqrt{(J \mp l_2 - 2)(J \pm l_2 + 1)}$$

Following Ref. [17], the Herman Wallis type function, $F(J, l_2, \Delta V, \Delta l_2)$, in Eq. (2.10) can be written as

$$F(J, l_2, \Delta V, \Delta l_2) = b_{\Delta V}^{|\Delta l_2|}m + d_{\Delta V}^{|\Delta l_2|}[J(J+1) + m - l_2^2] \quad (2.11)$$

for transitions involving $\Delta l_2 = 0$ matrix elements, and

$$F(J, l_2, \Delta V, \Delta l_2) = \quad (2.12)$$
$$-\frac{1}{2}\left(b_{\Delta V}^{|\Delta l_2|} + 2a_{\Delta V, l_2}^{|\Delta l_2|}\right)(2l_2\Delta l_2 + 1) + q_{\Delta V}^{|\Delta l_2|}\left[J(J+1) - l_2^2 - \Delta l_2\left(l_2 + \frac{\Delta l_2}{2}\right)\right]$$

for *Q*-branch transitions involving $\Delta l_2 = \pm 1$ matrix elements, and

$$F(J, l_2, \Delta V, \Delta l_2) = \quad (2.13)$$
$$-\frac{1}{4}\left(q_{\Delta V}^{|\Delta l_2|} - d_{\Delta V}^{|\Delta l_2|}\right) - \frac{1}{2}\left(b_{\Delta V}^{|\Delta l_2|} + q_{\Delta V}^{|\Delta l_2|} + 2a_{\Delta V, l_2}^{|\Delta l_2|}\right)(2l_2\Delta l_2 + 1)$$
$$-q_{\Delta V}^{|\Delta l_2|}l_2^2 + b_{\Delta V}^{|\Delta l_2|}m + d_{\Delta V}^{|\Delta l_2|}m^2 + \left(q_{\Delta V}^{|\Delta l_2|} - d_{\Delta V}^{|\Delta l_2|}\right)m\left(l_2\Delta l_2 + \frac{1}{2}\right)$$

for *P*- and *R*-branches of the same band. Here m = -J, 0, J+1 for *P*-, *Q*- and *R*-branches, respectively.

The $M_{\Delta V}^{|\Delta l_2|}$, $\kappa_{\Delta V,i}^{|\Delta l_2|}$, i= 1,2,3, $b_{\Delta V}^{|\Delta l_2|}$, $d_{\Delta V}^{|\Delta l_2|}$, $a_{\Delta V,l_2}^{|\Delta l_2|}$, and $q_{\Delta V}^{|\Delta l_2|}$ parameters in Eqs. (2.10-13) describe the strengths of all lines of cold and hot bands. For Δl_2 = ±2, the $\kappa_{\Delta V,i}^{|\Delta l_2|}$, $b_{\Delta V}^{|\Delta l_2|}$, $d_{\Delta V}^{|\Delta l_2|}$, $a_{\Delta V,l_2}^{|\Delta l_2|}$, and $q_{\Delta V}^{|\Delta l_2|}$ parameters are set to zero. The dimension of all EDM parameters is Debye. Note that Eq (2.10) is a linear combination of the EDM parameters.

For a polyad model of H^{eff}, each J, C matrix is block-diagonal with respect to the polyad number P. This means that each eigenfunction is non-zero within a single polyad and Eq (2.9) reads

$$< \Psi_f^{eff} \left| \mu_Z^{eff} \right| \Psi_i^{eff} >= \sum_{V_1',V_2',l_2',V_3' \in P'} \sum_{V_1'',V_2'',l_2'',V_3'' \in P''} T_{V_1',V_2',l_2',V_3'}^{J_i C_i} T_{V_1'',V_2'',l_2'',V_3''}^{J_i C_i} \times \qquad (2.14)$$

$$< V_1', V_2', |l_2'|, V_3', J_f, C_f \left| \mu_Z^{eff} \right| V_1'', V_2'', |l_2''|, V_3'', J_i, C_i >,$$

where P_i and P_f are the polyads of the initial and final state, respectively. Eq (2.14) defines the polyad EDM model. All EDM parameters depend only on the $\Delta V = \left(V_1^f - V_1^i, V_2^f - V_2^i, V_3^f - V_3^i\right)$ vector. This means that line strengths of all transitions with the same ΔP value are determined by a single set of EDM parameters.

Our non-polyad model slightly differs from the polyad model presented in Ref. [16]. The latter is non-linear with respect to the EDM parameters others than $M_{\Delta V}^{|\Delta l_2|}$, since the matrix element is proportional to

$$< V_1', V_2', |l_2'|, V'_3, J_f, C_f \left| \mu_Z^{eff} \right| V_1'', V_2'', |l_2''|, V_3'', J_i, C_i > \sim$$

$$M_{\Delta V}^{|\Delta l_2|} \left[1 + \sum_{\alpha=1}^{3} \kappa_{\Delta V,\alpha} V_\alpha + F(J, l_2, \Delta V, \Delta l_2) \right].$$

Our model is linear with respect to all EDM parameters. This allows us to calculate easily the derivatives $\frac{\partial < \cdots \left| \mu_Z^{eff} \right| \ldots >}{\partial x}$, where x is an EDM parameter. This is an important advantage in fitting the EDM parameters to observed line intensities.

In the polyad model, the dimension of the $M_{\Delta V}^{|\Delta l_2|}$ parameters is Debye while all the other parameters are dimensionless while in the present non-polyad model, the dimension of all parameters is Debye. Note that the $M_{\Delta V}^{|\Delta l_2|}$ parameters have the same values in the polyad and non-polyad models. For other parameters the non-polyad and polyad EDM parameters are related by the following simple relation: $x_{nonpol} = M_{\Delta V}^{|\Delta l_2|} x_{pol}$.

3. $^{14}N_2{}^{16}O$ line intensities data file

The transition database used as input data includes measured line intensities collected from the literature [18-50]. Most data were obtained by Fourier transform Spectroscopy (FTS), and Cavity Ring Down Spectroscopy (CRDS). There is also a bulk of calculated line positions of 144 bands, including 319 sub-bands, compiled by Toth [4] and called the SISAM.N2O line list. The SISAM line positions and intensities were calculated using empirical parameters obtained from a band-by-band fit of FTS measurements. The SISAM.N2O list contains a lot of bands whose line intensities were not reported elsewhere. It is thus suitable to combine in a single input data file the SISAM.N2O list and all literature measurements. An important issue is how to associate realistic uncertainties to the calculated SISAM.N2O line intensities. SISAM.N2O intensities are given in units of cm^{-2}/atm at 296K. The band intensities, S_v, cover the 10^{-6} - 10^{2} cm^{-2}/atm range. We adopted a two-stage algorithm to calculate the SISAM uncertainties: *(i)* for each band, we set band uncertainty unc_{band} in percent as 2, 3, 5, 10, 20, 30, 50, and 100 for bands with integer part of $log10(S_v)$ equal 2, 1, 0, -1, -2, -3, -4, and -5, respectively. The S_v values are given in Table 2 of Ref. (4). This guarantees that the weaker the band is, the larger the uncertainty of its line intensities is, *(ii)* within a given band, the uncertainties of the *P*, *Q*, and *R* lines are calculated according to the expression

$$unc_{line}^{branch} = unc_{band}\left[1 + \frac{1}{3}\ln\left(\left|J_{lower}^{branch} - J_{\max}^{branch}\right|\right)\right], \qquad (3.1)$$

where ln is the natural logarithm, J_{lower}^{branch} is the lower state rotational quantum number, and $J_{\max}^{branch}$ is the *J* value of a branch at which the branch intensity achieves the maximum intensity value. The factor 1/3 controls the rate at which the line uncertainty increases as the difference $\left|J_{lower}^{branch} - J_{\max}^{branch}\right|$ increases. This algorithm is, of cause, rather arbitrary but it provides a reasonable balance between the uncertainties of the measured intensities and those of SISAM.N2O. As a result, the SISAM.N2O uncertainties range between 3% and 100% while the mean value is about 27%.

The exhaustive list of the sources used as input data of the non-polyad EDM parameters is presented in **Table 1**.

Table 1.

Summary of the sources of the line intensities used as input data of the non-polyad EDM parameters. The sources are listed in chronological order.

Source	Technique [a]	N^k	Range (cm^{-1})	S_{min}-S_{max} (cm/molecule)	U_{min}-U_{max} (%)	T(K)
Lacome et al [18]		35	903.8 - 965.9	8.32E-24 - 4.65E-23	10.0	300
Lacome et al [19]	CTS	132	4944.3 - 5127.2	1.09E-24 - 1.08E-22	3.0	300
Levy et al [20]	FTS	159	1134.4 - 1327.4	5.25E-22 - 1.91E-19	5.0	295
Toth [21]	FTS	54	1133.5 - 1236.6	1.42E-24 - 2.43E-23	10.	296
Loewenstein et al [22]	TDLS	6	2168.7 - 2206.7	7.06E-21 - 8.86E-19	2.0	297
HITRAN1986 [23]	CALC	11	0.8 - 9.2	6.98E-26 - 7.27E-23	20.	296
Varanasi et al [24]	TDLS	7	1249.7 - 1279.0	2.89E-20 - 1.54E-19	2.0	295
Tang et al [25]	TDLS	5	1142.2 - 1180.9	2.25E-21 - 5.70E-21	3.0	296
Toth [26]	FTS	2977	1108.9 - 3515.7	1.05E-25 - 1.02E-18	1.4 - 30.0	296
Toth[b] [26]	FTS	181	1836.6 - 2375.4	2.63E-24 - 4.69E-22	3.0 - 6.1	296
Sirota et al [27]	TDLS	15	465.1 - 465.5	4.76E-26 - 7.42E-26	5.0	380 - 421
Rachet et al [28]	FTS	153	2635.8 - 3078.3	5.70E-25 - 4.53E-24	2.2	296
Rachet et al [29]	FTS	253	2413.9 - 2831.8	8.11E-24 - 1.20E-21	2.2	296
Azizi et al [30]	FTS	301	2386.1 - 2606.1	6.97E-24 - 2.34E-20	2.2	296
Chance et al [31]	CALC	340	2.5 - 45.3	4.65E-26 - 3.12E-22	20.0	296
Johns et al[c] [32]	FTS	105	554.7 - 631.8	4.19E-22 - 1.43E-20	2.2 - 30.1	300
Johns et al[d] [32]	FTS	98	547.4 - 635.2	2.04E-22 - 1.11E-20	1.4 - 8.9	300
Weber et al [33]	FTS	96	557.2 - 616.0	1.75E-22 - 7.78E-22	3.6 - 12.1	303
Régalia et al [34]	FTS	178	2439.6 - 3507.3	1.21E-22 - 3.46E-20	2.0 - 3.4	296
Toth[e] [35]	FTS	895	3676.9 - 7795.2	8.82E-26 - 1.45E-21	2.2 - 15.1	296
Toth[f] [35]	FTS	540	4553.1 - 7231.4	1.01E-25 - 1.05E-22	2.2 - 15.1	296
Claveau [36]	FTS	79	2129.9 - 2363.2	4.71E-25 - 2.50E-23	3.5	300
Daumont et al [37]	FTS	561	3895.5 - 4796.2	1.43E-26 - 1.92E-24	2.7 - 85.0	296
Daumont et al[g] [5]	FTS	156	1058.9 - 1238.6	1.52E-25 - 1.36E-23	2.0 - 7.0	297.6
Daumont et al[h] [5]	FTS	343	900.9 - 1221.5	1.52E-25 - 5.54E-21	5.0	296
Fukabori et al [38]	FTS	103	3422.1 - 3510.5	5.50E-22 - 3.45E-20	5.0 - 50.2	296
Parkes et al [39]	CRDS	8	6540.7 - 6578.3	6.90E-24 - 2.29E-23	5.4 - 11.0	296
Nemtchinov et al [40]	FTS	41	2224.6 - 2252.1	1.02E-19 - 9.93E-19	3.0	296
Fukabori et al [41]	FTS	85	3322.3 - 3396.2	1.08E-22 - 1.62E-21	1.9 - 41.4	296
Wang et al [42]	FTS	447	6718.5 - 7576.0	1.96E-26 - 8.33E-25	10.0	296
Daumont et al [43]	FTS	3358	5465.2 - 10173.7	3.48E-27 - 2.07E-23	1.0 - 99.0	296
Grossel et al [44]	QCLS	5	1275.5 - 1279.0	1.03E-19 - 1.41E-19	1.0	296
Aenchbache et al [45]	THz TDS	44	8.4 - 44.3	3.90E-23 - 3.15E-22	3.4 - 20.5	296
Milloud et al [46]	ICLAS	91	12804.6 - 12899.2	1.24E-28 - 1.04E-26	20.0	296
Toth [4]	CALC	29141	525.5 - 7232.3	2.02E-25 - 3.08E-20	2.0 - 100.0	296
Karlovets et al [47]	CRDS	1245	7018.3 - 7652.5	1.31E-29 - 7.66E-25	3.0 - 38.0	296
Karlovets et al [48]	CRDS	2631	7915.8 - 8331.5	1.02E-30 - 2.02E-25	5.0 - 20.0	296
Bertin et al [49]	CRDS	2130	5696.2 - 5908.0	4.27E-29 - 5.00E-25	3.0 - 15.0	296
Odintsova et al [50]	OFLAS	16	4980.6 - 4984.3	2.65E-25 - 6.23E-24	1.0	296 - 298
Karlovets et al [51]	CRDS	2739	8325.8 - 8622.1	3.81E-30 - 1.19E-25	3.0 - 20.0	296
Adkins et al[i] [52]	FARS-CRDS	177	6248.8 - 6398.3	7.60E-26 - 3.13E-24	1.1 - 26.7	296
Adkins et al[j] [52]	FARS-CRDS	177	6248.8 - 6398.3	5.60E-26 - 3.09E-24	1.2 - 30.4	296
Karlovets et al [53]	CRDS	3125	8321.8 - 8619.6	6.51E-31 - 1.16E-25	3.0 - 20.0	296
Karlovets et al [54]	CRDS	2405	7647.5 - 7986.6	3.70E-30 - 3.20E-24	3.0 - 20.0	296

Notes

[a] CTS - Czemy-Turner-type Spectrometer, TDLS - Tunable Diode Laser Spectroscopy, FTS - Fourier Transform Spectroscopy, QCLS - Quantum Cascade Laser Spectrometer, THz TDS - Terahertz Time-Domain Spectroscopy, ICLAS - IntraCavity Laser Absorption Spectroscopy, CRDS - Cavity Ring Down Spectroscopy, OFLAS - Optical Feedback Laser Absorption Spectroscopy, FARS-CRDS - Frequency-Agile Rapid Scanning Cavity Ring Down Spectroscopy,

[b] high pressure results,

[c] measurements performed at National Research Council of Canada,

[d] measurements performed at Kitt Peak National Observatory,

[e] Table 5,

[f] Table 4,

[g] Measurements performed in Paris,

[h] Measurements performed in Reims,

[i] speed dependent Voigt profile was used,

[j] Voigt profile was used,

[k] Total number of intensity values provided in the considered source.

Column 1 of **Table 1** provides references to data sources ordered according to the date of publication. Column2 gives the technique used for measurements (see details in the footnotes of the table). The measured data were supplemented with the calculated line

intensities taken from Toth's line list SISAM.N2O [4], HITRAN92 [23], and SAO database [31]. These sources are labeled as CALC in the second column. The number of lines, ranges of line position, *v*, and line intensity, *s*, are given in columns 3, 4, and 5, respectively. The measurement uncertainties (%) and temperatures (K) are listed in columns 6 and 7. If explicit uncertainty values were given in the publication, they were used. Otherwise, the listed values correspond to estimates based on the information given in the publication. The rationale for including the microwave calculated data in the input file is the unavailability of published measured data for the 0110-0110, 0200-0200, and 0220-0220 bands. **Fig. 1** shows an overview of the SISAM and measured sets of transitions used for the fit. Overall, the whole dataset gathers more than 55600 entries including more than 29100 SISAM calculated intensities (relying on FTS measurements). The number of measured FTS entries is about 11160 while about 14800 line intensities were obtained by CRDS. The weakest FTS and SISAM intensities are on the order of 10^{-25} cm/molecule while the high sensitivity of the CRDS technique allowed measuring much weaker lines (down to 10^{-30} cm/molecule) in the 5700-8600 cm^{-1} spectral interval.

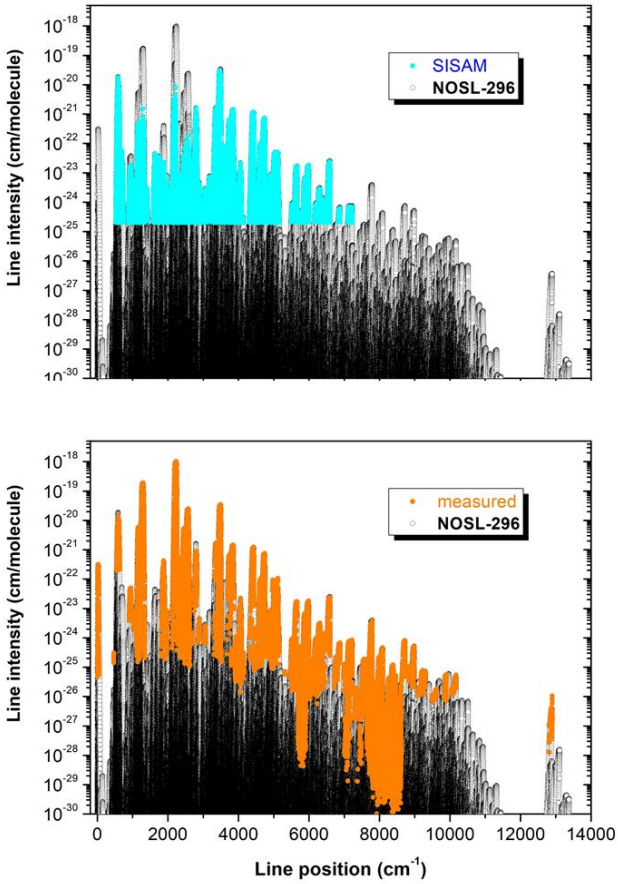

Fig. 1.

Overview of the line list of $^{14}N_2{}^{16}O$ transitions from the literature whose intensities were used as input data of the fit of the non-polyad effective dipole moment: SISAM (calculated) data and measurements (upper and lower panel, respectively).

4. Least-squares fits

In this section, we present the result of the least-squares fit of the experimental line positions and intensities using the non-polyad effective operator model.

According to Eq (2.9), the calculation of the transition moment requires the knowledge of the eigenfunctions. In this work, we use the eigenfunctions of the non-polyad EH model developed in Ref. [13]. Since the publication of this model, new measurements of line positions have become available [51,53,54,55]. The recent measurements were included in the line position data file presented in Ref. [13] and used to refine the non-polyad EH parameters. The dimensionless weighted standard deviation of the fit was 1.69 (compared to 1.71 in Ref. [13]), the number the fitted data was increased to 71,045 (56,888 in Ref. [13]), and 199 EH parameters were determined (195 in Ref. [13]). The partition function, *Q(T)*, required to compute the line intensities [Eq (2.1)] was taken from Ref. [56].

The procedure of the fit of the non-polyad EDM parameters minimizes the value of the dimensionless weighted standard deviation, χ, defined according to the usual formula

$$\chi = \sqrt{\frac{1}{N-n}\sum_{i=1}^{N}\left(\frac{r_i}{\delta_i}\right)^2}, \tag{4.1}$$

where

$$r_i = \frac{1}{2}\left(\frac{S_i^{obs}}{S_i^{calc}} - \frac{S_i^{calc}}{S_i^{obs}}\right) \tag{4.2}$$

is the symmetrized intensity residual of the *i*th line, $S_i^{obs}$and S_i^{calc} are observed and calculated values of the intensity of the *i*th line, respectively, δ_i is the measurement uncertainty of *i*th line in percent, *N* is the number of fitted line intensities, and *n* is the number of adjusted EDM parameters. Due to the lack of information on real experimental uncertainties of line intensity values in the vast majority of sources, it is convenient to use the following *RMS* value (in percent) to characterize the quality of a fit:

$$RMS = \sqrt{\frac{1}{N}\sum_{i=1}^{N} r_i^2} \tag{4.3}$$

The transitions of our intensity database belong to the ΔP=0-16, 18, and 24 series. Their intensities were fitted simultaneously in order to derive a single set of the EDM parameters. In total, 27,639 measured and 24,337 calculated line intensities were fitted using 152 EDM parameters leading to χ and *RMS* values of 1.28% and 14.7%, respectively.

The choice and significance of the parameters, along with their values, were analyzed using the singular numbers s_α and the right eigenvectors V_α of the dimensionless N-by-n Jacobi matrix J:

$$J_{i,\alpha} = \frac{x_\alpha}{\delta_i}\frac{\partial r_i}{\partial x_\alpha},\ i=1,2,\ldots,N;\ \alpha=1,2,\ldots,n \qquad (4.4)$$

The linear combinations $\sum_{\beta=1}^{n} c_{\alpha\beta}\, x_\beta$ of the fitted parameters x, corresponding to large singular numbers, are well determined from the fitted data. Here $c_{\alpha\beta}$ are the components of the right eigenvector V_α, which corresponds to the singular number s_α. These combinations are important for the model and are called "stiff" combinations [57]. In contrast, the linear combinations corresponding to small singular numbers have little effect on the behavior of the model. These unimportant parameter combinations are referred to as "sloppy". The usefulness of the singular number analysis is illustrated in **Fig. 2**.

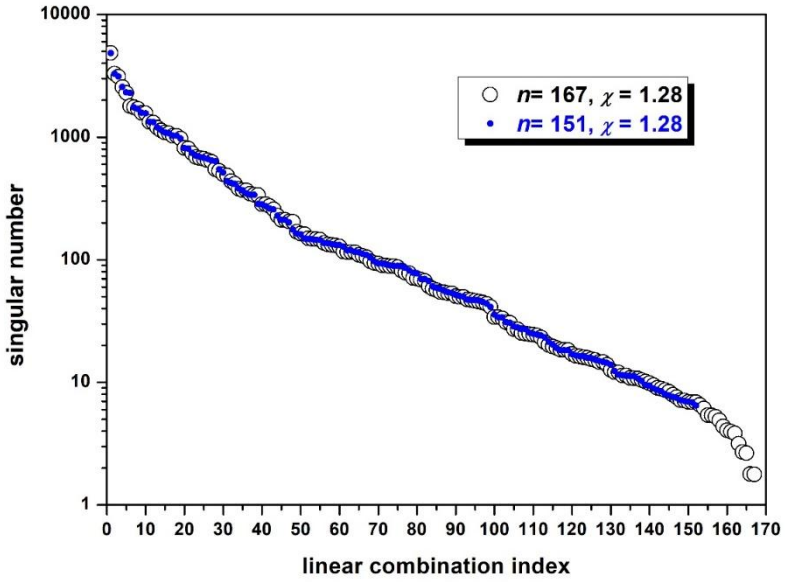

Fig. 2.
The singular numbers of the dimensionless Jacobi matrix of the fitted non-polyad EDM model. Open circles and dots correspond to the initial and final fit of the parameters (see Text).

During a preliminary stage of the fit we obtained χ= 1.28 with a set of 167 parameters. All parameters were statistically significant *i.e.* $x/\Delta x > 1$, where Δx is the standard error of the parameter x. The corresponding singular numbers of the J matrix are plotted as hollow circles in **Fig. 2.** It is seen that the curve consists of three parts. The first one consists of the five largest singular numbers. The linear combinations corresponding to these numbers include the

$M^0_{3,0,1}$, $M^0_{1,0,0}$, $M^0_{0,0,1}$, $M^0_{2,0,0}$, $M^0_{1,0,1}$, and $M^1_{1,1,1}$ parameters. These parameters are involved in stiff combinations and determine the core of the model. Most other parameters belong to a series with a log-linear behavior. The third part of the curve (above 160) exhibits a sharp decay. The parameters corresponding to these singular numbers belong to sloppy combinations. They are responsible for less important features of the model. As a result, it was decided to exclude 16 parameters corresponding to sloppy combinations and the EDM parameters were refitted. We got practically the same χ value with 151 parameters. Since the modified model has fewer parameters, it is expected to have better extrapolation capabilities than the initial model. Overall, we found that the singular value decomposition of the Jacobi matrix provides a very useful tool for analyzing the relative importance of the parameters of the model.

Overall, over a total number of 55,645 intensity values, 51,589 and 4,056 intensity values were included and excluded, respectively. The intensity data from Refs. [5(Paris),18-20,22,38,41] were excluded as their residuals r_i show considerable systematic deviations from zero. We also removed a number of lines from other sources. Most of these lines are marked by experimentalists as badly measured, blended, or have unresolved *e/f* splitting. The SISAM.N2O calculated bands below 900 cm^{-1} were also excluded since, according to Ref. [4], the rotational dependence of these bands is that of the v_2 band centered at 588 cm^{-1}, whose dependence was taken from Ref. [32].

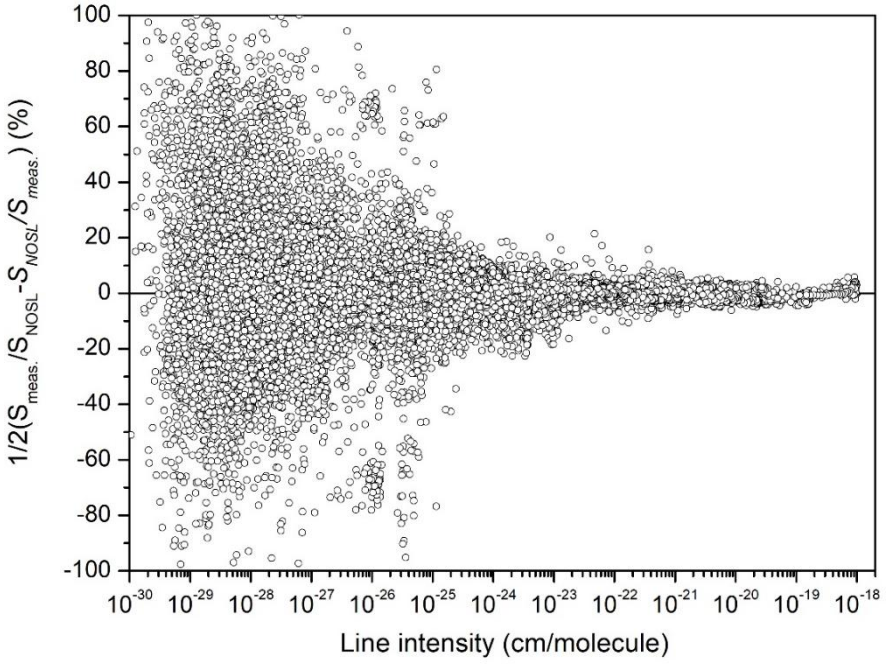

Fig. 3.

Symmetrized intensity residuals of the line intensities used to derive the non-polyad EDM parameters *versus* their intensity value. Transitions excluded from the fit are not plotted. The Y-axis is limited by ±100%.

The fitted model reproduces most of the measured intensities within their experimental uncertainties. This is illustrated in **Fig. 3** where the symmetrized intensity residuals, r_i – see Eq. (4.2), are plotted *versus* the measured intensity values.

5. The NOSL-296 line list

The fitted EH and EDM models presented in Section 4 were used to elaborate the NOSL-296 room temperature line list of $^{14}N_2{}^{16}O$ which is freely available at https://ftp.iao.ru/pub/LTS/NOSL-296/. The list covers the 0.02 – 13,378 cm^{-1} frequency range with the following parameters: maximum polyad number P_{max}= 24, maximum rotational quantum number J_{max}=150, maximum lower level energy E_{max}^{lower}=8,000 cm^{-1}, frequency range 0-15,000 cm^{-1}, reference temperature T_{ref} = 296 K, intensity cutoff I_{cut} = 10^{-30} cm/molecule, and isotopic abundance of 0.9903. An overview of the NOSL-296 is presented in **Fig. 4**. Note that, due to missing intensity measurements, the EDM parameters of the very weak high energy transitions with ΔP = 17, 19-23 could not be fitted and the corresponding transitions are thus missing in our list (mostly above 11000 cm^{-1} – see **Fig. 4**). The $V_1V_2l_2V_3$ vibrational assignment included in the list corresponds to the maximum value of the mixing coefficients, $T^{JC}_{V_1,V_2,|l_2|,V_3}$ [see Eq (2.9)]. The maximum values of J, V_1, V_2, l_2, and V_3 are 122, 9, 19, 10, and 6, respectively. Estimated uncertainties of the line positions and intensities for the lines having intensities greater than 10^{-25} cm/molecule are 0.001-0.01 cm^{-1} and 5-20 %. For weak lines these uncertainties may reach 0.1 cm^{-1} and 100 %.

The format of the NOSL list is presented in **Table 2**. The format and units of the line position, intensity and lower state energy are identical as those used in the HITRAN database. Each energy level has two assignments. The first one is based on the dominant normal mode and is similar to that given in the HITRAN2020 list. It includes six integer numbers: V_1,V_2,$|l_2|$,V_3,J,C entering in Eq (2.4). The second one includes the three integer numbers: J,C,N defined in Eq. (2.5). The first assignment is not unique as, due to couplings, a same normal mode may be dominant in the eigenfunctions of various vibrational states. On the contrary, the second assignment provides a one-to-one correspondence between J,C,N and eigenvalues. The end of each record consists of two parts of variable length. The first part bracketed by '|' and '||' symbols, includes up to four pairs of numbers. The first one is the V_1,V_2,$|l_2|$,V_3,C vibrational assignment of the dominant basis function of the upper state. The second one is the absolute value of the mixing coefficient T which enter in Eq. (2.8). The

second pair (if any) has similar information about the next largest contribution. The maximal number of such pairs is four. The last part bracketed by '||' and end of record gives similar information for the lower state

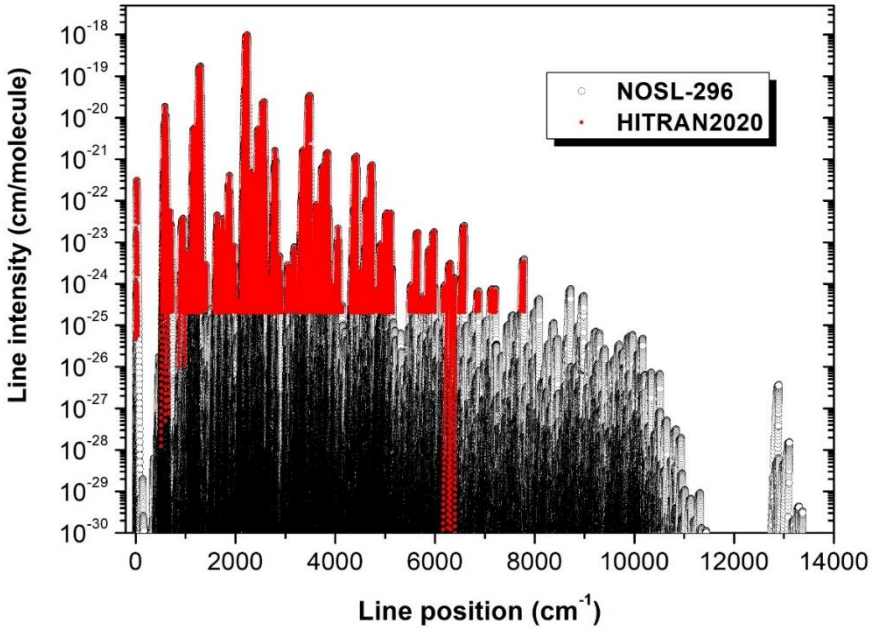

Fig. 4.

Overview of the NOSL-296 line list of $^{14}N_2{}^{16}O$ and comparison to the HITRAN2020 line list.

Symbol	Parameter	Field length	Data type	Comments or units
ν	Line position	12	real	cm^{-1}
S	Line intensity	10	real	cm/molecule at 296 K
$E"$	Lower state energy	12	real	cm^{-1}
V'_1	Upper state vibrational quantum numbers	3	integer	
V'_2		2	integer	
l'_2		2	integer	
V'_3		2	integer	
C'		1	integer	
$V"_1$	Lower state vibrational quantum numbers	3	integer	
$V"_2$		2	integer	
$l"_2$		2	integer	
$V"_3$		2	integer	
$C"$		1	integer	
branch	branch	2	character	'P', 'Q', 'R'
$J"$	lower state J	4	integer	
$w"$	lower state Wang symmetry	1	character	'e' or 'f'
J'	upper state J	4	integer	
C'	upper state Wang symmetry	2	integer	1 for 'e' states 2 for 'f' states
N'	upper state eigenvalue number	4	integer	
$J"$	lower state J	4	integer	
$C"$	lower state Wang symmetry	2	integer	1 for 'e' states 2 for 'f' states
$N"$	lower state eigenvalue number	4	integer	

|…| ||…end of record	upper state eigenvector decomposition lower state eigenvector decomposition			See text See text

Table 2.
Description of the parameters and the format of the NOSL-296 list

6. Comparison with Ames-296 and HITRAN2020 line lists

Ames-296

The Ames-296 line list [12] is available at http://huang.seti.org with file name n2o.6iso.296K.1E-31.15Kcm-1.Y02-A8.dmsC.dat. The line list includes 6 isotopologues in natural isotopic abundance. It was computed with the following parameters: maximum upper state energy E_{max}^{lower} = 20,000 cm^{-1}, reference temperature T_{ref} = 296 K, intensity cutoff I_{cut} = 10^{-31} cm/molecule. For comparison purpose with NOSL-296, we first extracted the $^{14}N_2{}^{16}O$ transitions with intensities greater than 10^{-30} cm/molecule. The line position range of the Ames-296 list extends up to 14,998 cm^{-1}. The number of Ames and NOSL lines are 837,939 and 889,509, respectively.

In the Ames list, each energy level is identified with the *J*, *P*, *S*, *N* numbers. The parity *P* and the symmetry *S* enable us to determine unambiguously the Wang parity, *C*, used for the assignments in NOSL-296. The *J, C, N* numbers, also used for our assignments, are identical to those defined in Eq (2.5). Therefore, a one-to-one correspondence could be established for most of the lines of the two lists. Out of 837,939 Ames-296 transitions, we were able to match 757,807 transitions (more than 90 %). The differences between Ames and NOSL line position presented in **Fig. 5**, show an overall good agreement with more than 92% position differences agreeing within ±0.1 cm^{-1}. We note however deviations approaching +1.5 cm^{-1} and -3.2 cm^{-1}. In principle, our EH model has an accuracy close to the experimental accuracy and provides more accurate transition frequencies than the Ames calculations based on an empirical PES. The excellent predictive ability of the EH model has been checked in the successive CRDS studies in the near infrared. For instance, in the very recent analysis of the CRDS spectrum in the 8325 and 8622 cm^{-1} region [53], most of the 2745 reported transitions of $^{14}N_2{}^{16}O$, were newly detected and the maximum position deviation of the predicted line position was limited to 0.048 cm^{-1}, the great majority of the measured line positions coinciding with the EH predictions within ±0.01 cm^{-1} (see Fig. 4 of Ref. [53]).

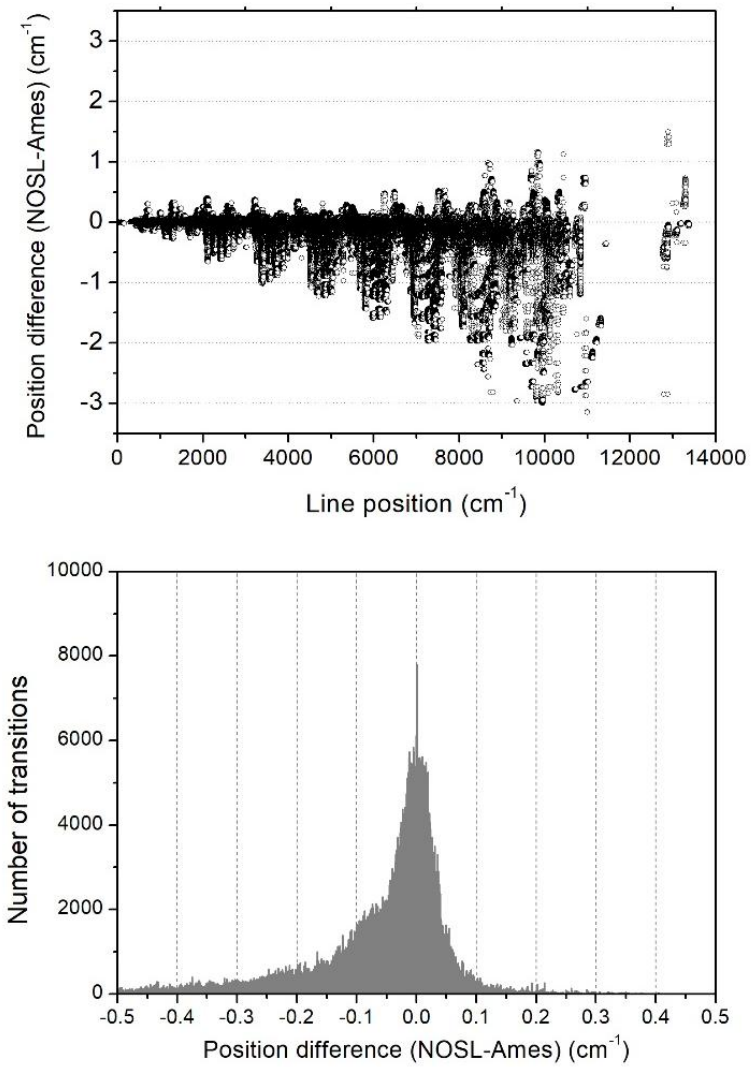

Fig. 5
Differences of the $^{14}N_2{}^{16}O$ transition frequencies in the NOSL-296 and Ames-296 lists and corresponding histogram.

The histogram of the deviations presented in the lower panel of **Fig. 5** confirms the slight systematic overestimation of the Ames position apparent on the upper panel (the median deviation is about 0.027 cm^{-1}).

As a test of the NOSL and Ames intensities, we present in **Fig. 6** a comparison to the set of intensity values used in the fit of the EDM parameters. Symmetrized intensity residuals are plotted for the two lists. Overall the agreement is good even if some significant deviations are noted for the strongest lines of the Ames list which have an intensity overestimated by about 3.5 %. In addition, there are two series of lines with line intensities as large as 10^{-21} cm/molecule have their Ames intensities underestimated by about 25 % (compared to measurements and NOSL). Namely, the *Q* branch lines of the 0110-0000 band with even *J*

values (the symmetrized intensity residuals are about 10%) and the 0002-0000 band (the symmetrized intensity residuals are about 30%). Interestingly, the *Q* branch lines of the 0110-0000 band with odd *J* values are in perfect agreement with NOSL values (the symmetrized intensity residuals are about 1%).

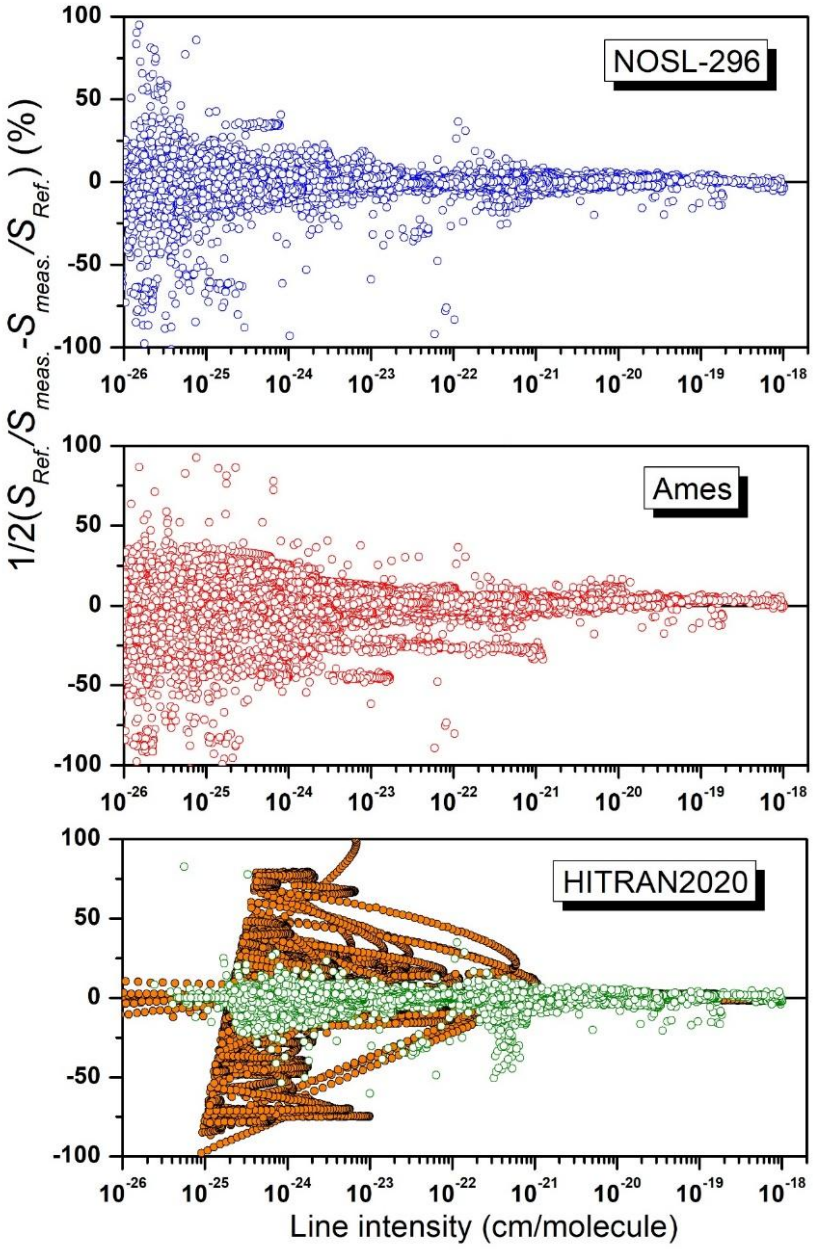

Fig. 6.

Symmetrized intensity residuals for the NOSL-296, Ames-296 and HITRAN2020 lists compared to the line intensities used to determine the non-polyad EDM parameters (blue, red and green open circles, respectively). On the lower panel, the NOSL-HITRAN symmetrized intensity residuals, $\frac{1}{2}\left(\frac{S_i^{NOSL}}{S_i^{HITRAN}} - \frac{S_i^{HITRAN}}{S_i^{NOSL}}\right)$, are plotted for comparison (orange dots).

HITRAN2020

The $^{4}N_{2}{}^{16}O$ list provided in HITRAN2020 incudes 33236 transitions, most of them transferred from the SISAM.N2O line list, as summarized in **Table 3**. The HITRAN intensity cutoff is 2×10^{-25} cm/molecule for most of the bands. This value is about five orders of magnitude larger than both the NOSL-296 intensity cutoff and the detectivity threshold of the most sensitive intensity measurements performed by CRDS (see **Fig. 1**).

Table 3.
Summary of the HITRAN2020 $^{14}N_{2}{}^{16}O$ sources.

Source	ν_{min}-ν_{max} (cm^{-1})	S_{min} - S_{max} (cm/molecule)	N [a]	Unc ν [b] (10^{-3} cm^{-1})	Unc S [c] (%)
Rothman et al. [23]	0.8-9.3	4.7×10^{-26} - 7.3×10^{-23}	51	unreported	unreported
Chance et al. [31]	10.0- 45.3	5.8×10^{-26} - 3.1×10^{-22}	300	unreported	unreported
Johns et al. [32]	508-672	1.2×10^{-28} - 1.8×10^{-20}	293	0.001 - 0.01	5 - 10
Daumont et al. [5]	872- 1246	1.0×10^{-26} - 3.7×10^{-23}	268	0.1 – 1.0	1 - 5
Adkins et al. [52]	6165-6405	1.0×10^{-30} - 2.1×10^{-25}	191	1.0 – 10.0	<1 - >20
Toth [4]	526-7797	2.0×10^{-25} - 1.0×10^{-18}	31996	0.1 – 1.0	2-5
Toth [58] [d] Adkins et al. [52]	6246-6396	2.1×10^{-25} - 3.1×10^{-24}	166	0.1	<1 - 5

Notes
[a] Number of transitions
[b] HITRAN2020 error bar on the line positions
[c] HITRAN2020 error bar on the line intensities
[d] Source for the line positions

Most of the HITRAN2020 line positions and line intensities are based on calculations performed by Toth [4]. Line positions were modeled with effective parameters of the vibration-rotation energy level. The vibration-rotation energy levels E_v belonging to vibrational state $V=(V_1,V_2,l_2,V_3,C)$ is modeled using the standard expression:

$$E_V(J) = G_V + B_V J(J+1) - D_V[J(J+1)]^2 + H_V[J(J+1)]^3 + L_V[J(J+1)]^4 \qquad (6.1)$$

and the line position of a transition is given by

$$\nu_{V,J\rightarrow V',J'} = E_{V''}(J'') - E_{V'}(J')$$

The spectroscopic constants G_v, B_v, D_v, H_v, L_v of the upper and lower states were fitted to the observed transition frequencies. The fitted values of these constants are given in Table 1 of Ref. [4]. There are several strongly perturbed bands for which the expansion (6.1) fails. In those cases, the measured values of the line positions were adopted in SISAM.N2O.

The line position residuals ν_{NOSL} - ν_{HITRAN} are plotted in **Fig. 7** as a function of the line position. Most residuals are rather small, within ±0.01 cm^{-1}. However, there are several bands whose residuals reach 0.1 cm^{-1}. All these bands originate from SISAM.N2O and have $l_2 > 3$.

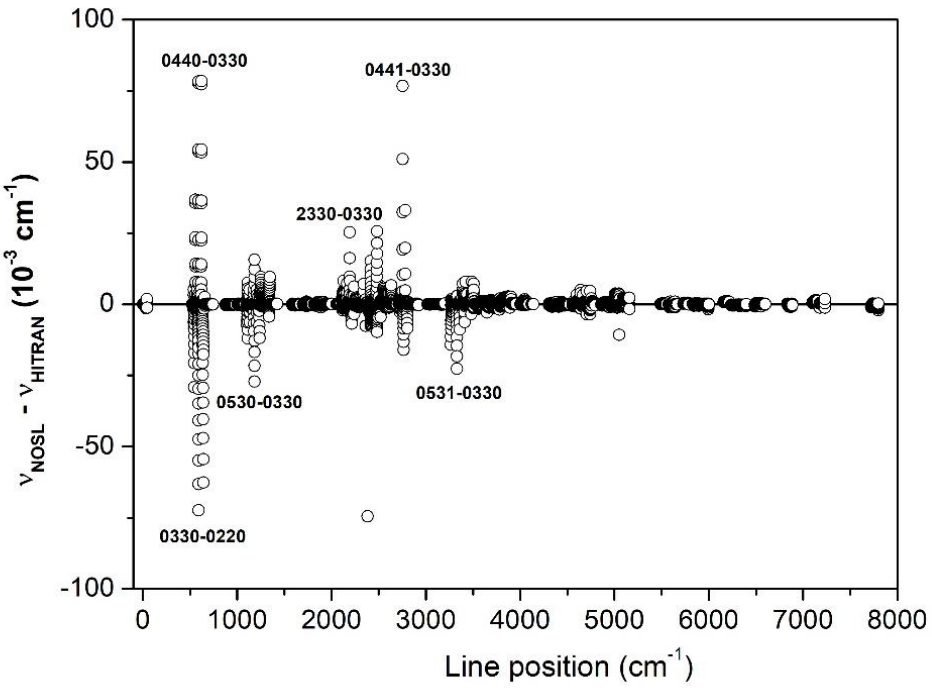

Fig. 7.

Line position differences (ν_{NOSL} - ν_{HITRAN}) between the presently constructed NOSL-296 line list of $^{14}N_2{}^{16}O$ and the HITRAN2020 database.

For the line strength, *S*, the following expression was used

$$S = S_v \frac{v}{v_0} L \left[1 - \exp\left(-\frac{v}{kT}\right)\right] \exp\left(-\frac{E_R}{kT}\right) \frac{F}{Q_R} \tag{6.2}$$

where S_v is the band intensity, v is the transition frequency, ν_0 is the band center, L is the square of the matrix element of the direction cosines connecting the upper state to the lower state, E_R is the lower state rotational energy, k is the Boltzmann constant, T is the temperature, and Q_R is the rotational partition function.

The band intensity S_v is expressed, in turn, as

$$S_v = \frac{8\pi^3}{3hcTQ_v} |R|^2 \nu_0 \exp(-\frac{E_V}{kT}) \tag{6.3}$$

where Q_v is the vibrational partition function, E_V is the lower state vibrational energy, and R is the matrix element of the rotationless electric-dipole moment. The L factor depends on J'', ℓ', ℓ'', and m, where $m = J'' + 1$ for the R-branch ($\Delta J = 1$), $m = -J''$ for the P-branch ($\Delta J = -1$), $m = 0$ for the Q-branch, ℓ is the vibrational angular momentum quantum number. The expressions for the L factor are given in Eq. (4) of Ref. [4]. Finally, the F-factor is expressed as:

$$F = [1 + a_1 m + a_2 J'(J'+1)]f \text{ for } P \text{ and } R \text{ branches, and} \tag{6.4}$$

$$F = [1 + a_3 J'(J'+1)]f \text{ for } Q \text{ branches,}$$

where $f=1$ for the $\Delta\ell = 0, \pm 1$ bands and $f=[J'(J'+1)]^2$ for the $\Delta\ell = 2$ bands.

Thus, SISAM.N2O J dependence of the calculated line positions and intensities are based on simple polynomial expressions (6.1-6.4). For a given band, line intensities in the P and R branches depend on the S_v, a_1, and a_2 parameters while the Q line intensities depend on S_v and a_3. The S_v, a_1, a_2, and a_3 parameters of each band were fitted to the FTS measured intensities (their values are given in Table 2 of Ref. [4]). Overall, the SISAM.N2O include 231 $^{14}N_2{}^{16}O$ bands but for 61 of them, only the band strength S_v is given and the corresponding a_i parameters were assumed to be null.

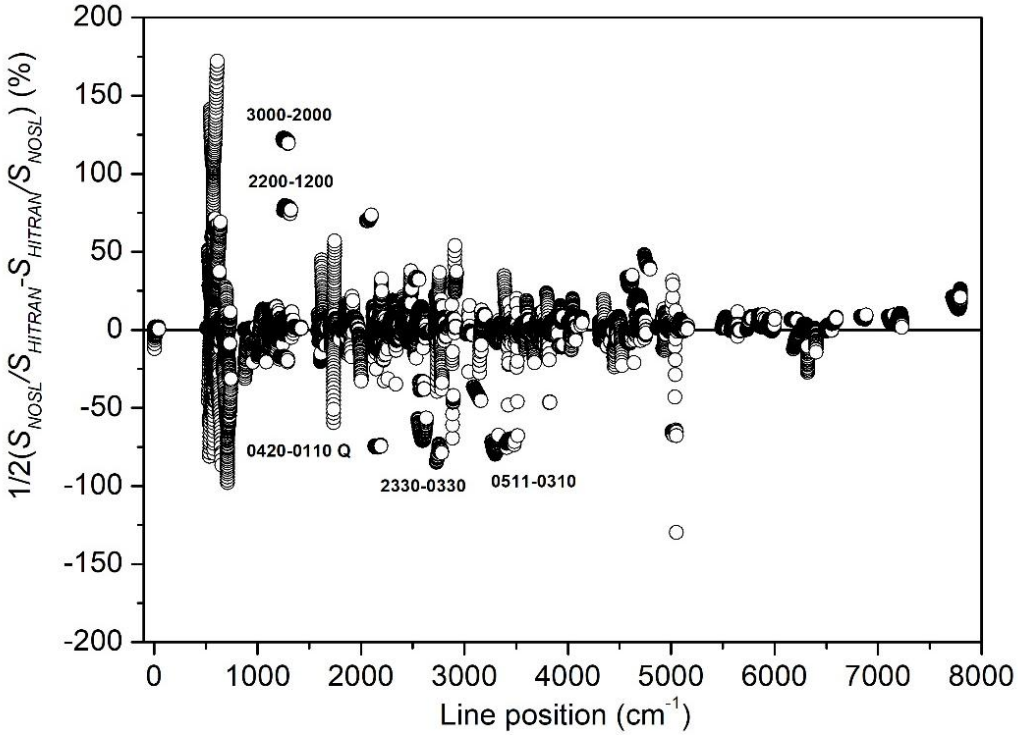

Fig. 8
Symmetrized intensity residuals of NOSL-296 and HITRAN2020 *versus* line positions.

As concerns line intensities, the NOSL-HITRAN symmetrized intensity residuals are plotted *versus* the line positions in **Fig. 8**. The bands below 900 cm^{-1} show largest residuals. According to Ref. [4], the values of S_v and a_1 parameters for the v_2 band centered at 588 cm^{-1} were taken from Ref. [32]. For other bands below 900 cm^{-1}, the a_i values were set equal to those of the v_2 band. Thus, all these bands have an identical rotational dependence. Estimates of S_v values were used for all these bands leading to large residuals in the 500 - 900 cm^{-1} region. The 3000-2000, 2200-1200, 0511-0310 bands marked in **Fig. 8** have intensities calculated with $a_1 = a_2 = a_3 = 0$ [4] which leads to deviations larger than a factor of two compared to our values.

Residuals between the measured and HITRAN line intensities are included on the lower panel of **Fig. 6** (green circles). Qualitatively, the distribution of the residuals is very similar to that obtained with NOSL. We note, however, a series of lines with intensities in the 10^{-22} - 10^{-21} range with HITRAN intensities largely underestimated. The lower panel of **Fig. 6** includes the NOSL-HITRAN residuals for the whole set of HITRAN data. Over a total of more than 33000 entries, 1500 HITRAN line intensities deviate by more than 50% compared to NOSL. About 600 of them correspond to the above discussed SISAM data in the 500 - 900 cm^{-1} region. The other ones above 900 cm^{-1} correspond to SISAM bands involving large values of the l_2 quantum number, for which only the S_v values were used for the SISAM intensity calculations (see Table 2 of Ref. 4).

7. Discussion and concluding remarks

Several experimental works have proven that the traditional modeling of the N_2O rovibrational spectrum in the framework of the polyad model of effective Hamiltonian neglects a number of interpolyad resonance interactions (in particular Coriolis interaction [35,48,49,51,59-62]. Consequently, a non-polyad model of the effective Hamiltonian was recently developed to account for the $^{14}N_2{}^{16}O$ line positions including those perturbed by interpolyad interactions [13]. The line intensities to be associated to the calculated line positions requires the development of a non-polyad model of the effective dipole moment which has been elaborated in the present work. The intensity modeling which uses eigenvalues and eigenvectors of the non-polyad effective Hamiltonian [13], has allowed reproducing a large set of more 50,000 intensity values collected in the literature, with accuracy consistent with the measurement uncertainties. The non-polyad models of the effective Hamiltonian and effective dipole moment were used to create the room-temperature line list of $^{14}N_2{}^{16}O$, NOSL-296. Almost 900,000 lines covering the 0.02-13,378 cm^{-1} spectral range are included in NOSL-296 above an intensity cutoff of 10^{-30} cm/molecule at 296 K.

The obtained line list was compared with HITRAN2020 [1] and Ames-296 line lists [12]. Although limited to lines with intensity larger than 2×10^{-25} cm/molecule, the HITRAN2020 line list, mostly relying on SISAM.N2O database by Toth, shows a number of deficiencies in particular in the 500 - 900 cm^{-1} region (see **Fig. 8**).

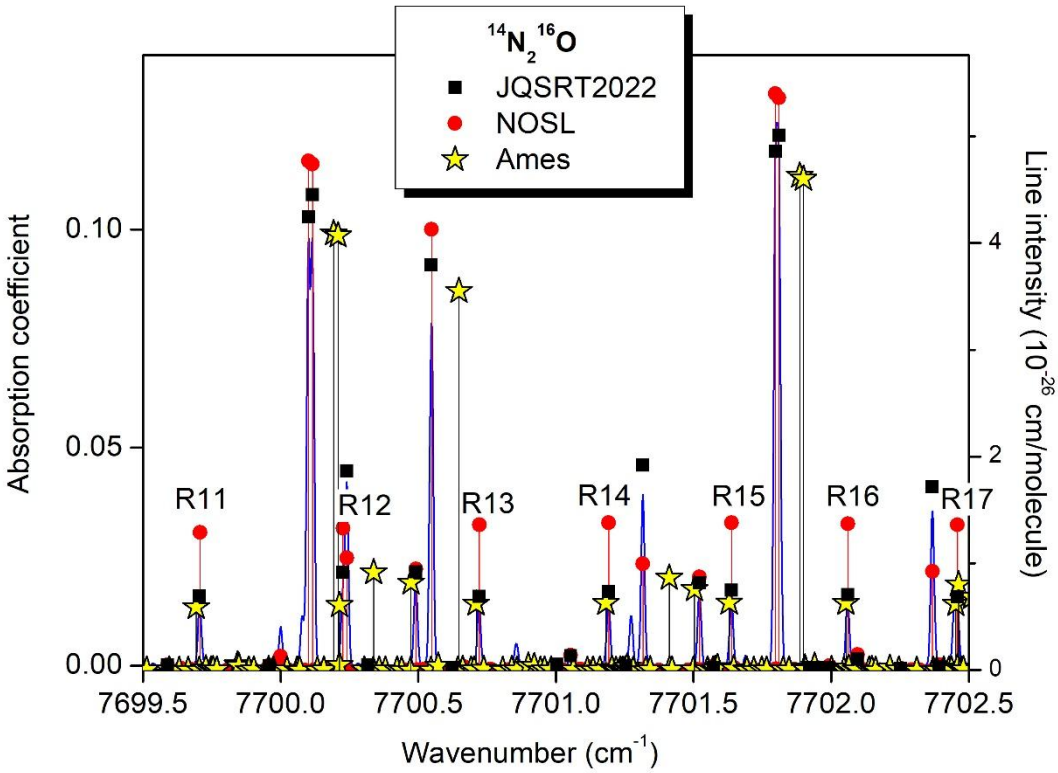

Fig. 9.

Superposition of the CRDS spectrum of natural nitrous oxide recorded at 1.0 Torr to the retrieved stick spectrum (black squares) [54], to the present NOSL list (red dots) and to the Ames theoretical line list of $^{14}N_2{}^{16}O$ (yellow stars) [12]. The *R*(*J*) assignments of the lines of the 2003e-1000e band are indicated.

The Ames line list [12] based on an empirical potential energy surface and a pure *ab initio* dipole moment surface has the advantage to be complete down to an intensity cutoff of 10^{-30} cm/molecule, the same as that of the NOSL list. Although the comparison of the NOSL and Ames lists shows an overall good agreement for the set of line intensities used for the fit of the non-polyad EDM parameters, the two lists show significant differences beyond the observations. Some general considerations on the respective advantages and drawbacks of the two lists are discussed below.

As concerns line positions, the accuracy of the Ames positions cannot compete with the NOSL position accuracy. NOSL positions relying on an empirical fit of a large set of measured positions have an accuracy close to the experimental accuracy, typically a few 10^{-3} cm^{-1}. The comparison presented in **Fig. 5** shows that Ames position uncertainties are one or two orders of magnitude larger. As an example, we present in **Fig. 9** the direct superposition of the NOSL and Ames stick spectra to the CRDS spectrum of natural nitrous oxide recently analyzed in Ref. [54]. In the displayed spectral interval near 7700 cm^{-1}, the Ames positions of

549 the five strongest lines are overestimated by 0.07-0.10 cm^{-1}. If we now consider the line
550 intensities of the same five lines, their Ames and NOSL values differ by about 10 %, the
551 experimental values being intermediate between Ames and NOSL values. On the same **Fig. 9**,
552 we have indicated the *R*(*J*) assignments of the lines of the 2003e-1000e band for which the
553 Ames intensities show an excellent agreement with the experimental values while NOSL
554 intensities are overestimated by about a factor of two. In order to illustrate the fact that this
555 situation is not general and that it is not possible to draw a general conclusion on the
556 recommended line intensities, we present in **Fig. 10**, the CRDS spectrum in the nearby region
557 of the 0203e-0000e band centered at 7665.2734 cm^{-1} [54]. While the NOSL line intensities
558 coincide with the measurements, the Ames intensities are systematically underestimated by
559 about 20 %. (Note that none of the lines presented in **Figs. 9** and **10** are included in the
560 HITRAN2020 database).

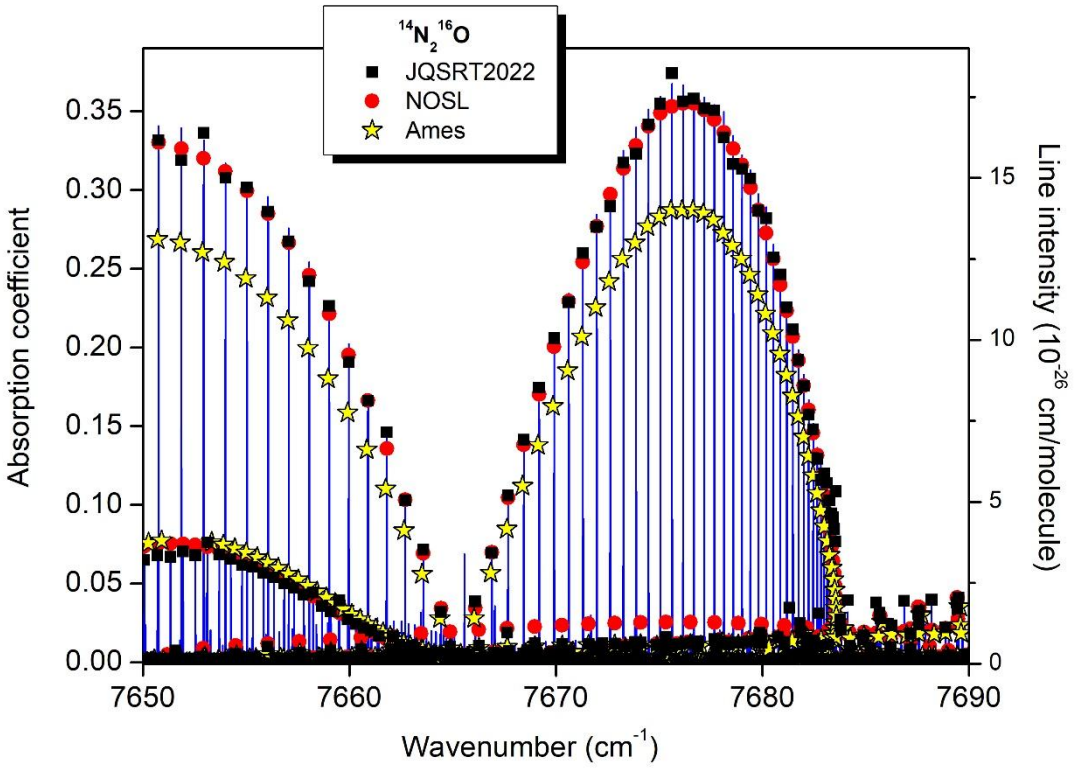

561

562 **Fig. 10.**
563 Intensity comparison for the 0203e-0000e band of $^{14}N_2{}^{16}O$.
564 Superposition of the CRDS spectrum of natural nitrous oxide to the corresponding
565 experimental stick spectrum (black squares) [54], to the present NOSL list (red dots) and to
566 the Ames theoretical line list (yellow stars) [12].

567 Thus, Ames and NOSL have specific advantages. The *ab initio* Ames dipole moment
568 surface enables, in principle, to predict the intensities of all bands (including those of the

minor isotopologues). This is not the case of the NOSL list for which the required EDM parameters depends on the availability of measurements in the literature. For instance, due to the lack of intensity information, the very weak high energy transitions with ΔP = 17, 19-23 are missing in the NOSL list. On the other side, when solid intensity information is available the fitted EDM reproduces most of the measured intensities with an accuracy consistent with the measurements (*e.g.* **Fig. 10**). The accuracy of the Ames intensities is strongly dependent on the empirical potential energy surface used to compute the eigenstates. In the case of weak interacting bands borrowing their intensity from a stronger partner, the accuracy of the eigenstates is critical. In those situations, in the case of carbon dioxide [63], the EH eigenstates proved to be more accurate than AMES eigenstates.

It is worth underlying that for a given ΔP series of transitions, the accuracy of the NOSL calculated intensities might strongly differ according to the band, because they depend on different EDM parameters. For instance, we are currently performing an intensity analysis of CRDS spectra in the 6950 - 7653 cm^{-1} interval for which the position analysis was reported in Ref. [62]. The 0004-1000 band belonging to ΔP = 14 series of transitions and centered at 7429.237 cm^{-1} is located in the studied region. The intensity of the 0004-1000 band is mainly determined by the $M^0_{-1,0,4}$ EDM parameter which could not be determined in the global fit of the EDM parameters used to generate NOSD intensities. As a result, NOSD predicted intensities are strongly underestimated by a factor of 9 compared to the observations while Ames intensities which are 8.5 larger than NOSL intensities, mostly coincide with the measured values.

In summary, the next generation of the line list should combine the advantages of the different approaches. We would recommend the positions of most transitions to be taken from the non-polyad EH model. The EH predicted positions have proven to be highly reliable to assign newly observed transitions. In case of a large set of accurate measurements of a given band, band-by-band spectroscopic parameters might be an alternative approach for line positions but the EH model has the advantage to provide accurate predictions beyond the observations. In the case of transitions involving levels in the vicinity of the dissociation limit, the Ames positions may become preferable.

At present, the optimal solution for line intensities appears to be a combination of NOSL and Ames calculated values. For the strong measured bands and strongly interacting bands NOSL values are preferable. For the bands not yet measured and for which the leading EDM parameters could not yet be determined (see the above example of the 0004-1000 band), the Ames intensity values should be preferred. The construction of a line list combining

NOSL and Ames intensities remains to be done. At the end of the process, serious validation tests against high quality spectra will be require ensuring that the best intensity source has been retained.

Acknowledgments

Sergey Tashkun acknowledges The Ministry of Science and Higher Education of the Russian Federation for financial support. We thank Dr. X. Huang for data sharing and helpful discussions. This project is supported by CNRS (France) in the frame of the International Research Project "SAMIA". Most of the computations presented in this paper were performed using the GRICAD infrastructure (https://gricad.univ-grenoble-alpes.fr), which is supported by Grenoble research communities.

References

1. Gordon IE, Rothman LS, Hargreaves RJ, Hashemi R, Karlovets EV et al., The HITRAN2020 molecular spectroscopic database. J Quant Spectrosc Radiat Transfer 2021;107949. doi: 10.1016/j.jqsrt.2021.107949.
2. Delahaye T, Armante R, Scott NA, Jacquinet-Husson N, Chédin A. et al., The 2020 edition of the GEISA spectroscopic database, J Mol Spectrosc 2021;380:111510, doi.org/10.1016/j.jms.2021.111510
3. Rothman LS, Jacquemart D, Barbe A., Benner D.C., Birk M. et al., The HITRAN 2004 molecular spectroscopic database, J Quant Spectrosc Radiat Transfer 2005;96:139-204.
4. Toth RA. Linelist of N2O parameters from 500 to 7500 cm^{-1}, http://mark4sun.jpl.nasa.gov.data/spec/N2O/.
5. Daumont L, Claveau C, Debacker-Barilly MR, Hamdouni A, Régalia-Jarlot L, Teffo JL, Tashkun SA, Perevalov VI. Line intensities of $^{14}N_2{}^{16}O$: the 10 micrometers region revisited. J Quant Spectrosc Radiat Transfer 2002;72:37-55.
6. Rothman LS, Barbe A, Benner DC, Brown LR, Camy-Peyret C, et al. The HITRAN molecular spectroscopic database: edition of 2000 including updates through 2001. J Quant Spectrosc Radiat Transfer 2003;82:5-44.
7. Rothman LS, Gordon IE, Barbe A, Benner DC, Bernath PF, et al., The HITRAN 2008 molecular spectroscopic database, J Quant Spectrosc Radiat Transfer 2009;110:533-72.
8. Rothman LS, Gordon IE, Babikov Y, Barbe A, Benner DC, Bernath PF, et al., The HITRAN 2012 molecular spectroscopic database, J Quant Spectrosc Radiat Transfer 2013;130:4-50.
9. Gordon IE, Rothman LS, Hill C, Kochanov RV, Tan Y, PF Bernath PF, et al., The HITRAN2016 molecular spectroscopic database. J Quant Spectrosc Radiat Transfer 2017;203:3-69. doi: 10.1016/j.jqsrt.2017.06.038.
10. Tashkun SA, Perevalov VI, Lavrentieva NN. NOSD-1000, The high-temperature nitrous oxide spectroscopic databank. J Quant Spectrosc Radiat Transf 2016;177:43–8. doi: 10.1016/j.jqsrt.2015.11.014.
11. Hargreaves RJ, Gordon IE, Rothman LS, Tashkun SA, Perevalov VI, Lukashevskaya AA, Yurchenko SN, Tennyson J, Müller HSP, Spectroscopic line parameters of NO, NO_2, and N_2O for the HITEMP database J Quant Spectrosc Radiat Transfer 2019;232:35-53.
12. Huang X, Schwenke DW, Lee TJ, Ames-1 296K IR line lists for N_2O isotopologues, The 75th International Symposium on Molecular Spectroscopy, Talk TC05.
13. Tashkun SA, Global modeling of the $^{14}N_2{}^{16}O$ line positions within the framework of the non-polyad model of effective Hamiltonian, J Quant Spectrosc Radiat Transfer 2019;231:88-101. doi 10.1016/j.jqsrt.2019.04.023
14. Perevalov VI, Lobodenko EI, Lyulin OM, Teffo J-L, Effective dipole moment and band intensities problem for carbon dioxide. J Mol Spectrosc 1995;171:435-52.
15. Lyulin OM, Perevalov VI, Teffo J-L, Effective dipole moment and band intensities of nitrous oxide J Mol Spectrosc 1995;174:566-80.
16. Tashkun SA, Perevalov VI, Teffo J-L, Tyuterev VlG, Global fit of $^{12}C^{16}O_2$ vibrational-rotational line intensities using the effective operator approach, J Quant Spectrosc Radiat Transfer 1999;62:571-98.
17. Watson JKG, Quadratic Herman-Wallis factors in the fundamental bands of linear molecules, J Mol Spectrosc 1987;125:428-41.
18. Lacome N, Boulet C, Arié E, Spectroscopie par source laser. III. Intensités et largeurs des raies de la Transition 0001-1000 du protoxyde d'azote. Ecarts à la forme de Lorentz. Can J Phys 1973;51:302-10.
19. Lacome N and Levy A. Line strengths and self-broadened linewidths of N_2O in the 2-μm region 2400-0000 and 0112-0000 transitions. J Mol Spectrosc 1981;85:205-14.
20. Levy A, Lacome N, Guelachvili G. Measurement of N_2O line strengths from high-resolution Fourier transform spectra J Mol Spectrosc 1984;103:160-75.
21. Toth RA, Line strengths of N_2O in the 1120-1440-cm^{-1} region. Appl Opt 1984;23:1825-34.

22. Loewenstein M, Podolske JR, Blackburn TE, Varanasi P, Diode laser measurements of line strengths and widths in the 4.5-μm bands of N_2O. J Quant Spectrosc Radiat Transfer 1986;35:231-5.
23. Rothman LS, Gamache RR, Goldman A, Brown LR, Toth RA The HITRAN database: 1986 edition, Appl Opt 1987;26:4058-97.
24. Varanasi P and Chudamani S. J Quant Spectrosc Radiat Transfer. 1989;41:359-62.
25. Tang LW, Nadler S, Daunt SJ. Tunable diode laser measurements of absolute line strengths in the $2v_2$ band of N_2O near 8μm. J Quant Spectrosc Radiat Transfer. 1989;41:97-101.
26. Toth RA. Line strengths (900-3600 cm^{-1}), self-broadened linewidths, and frequency shifts (1800-2360 cm^{-1}) of N_2O. Appl Opt 1993;32:7326-65.
27. Sirota JM and Reuter DC. Absolute intensities for the Q-branch of the $3v_2 \leftrightarrow v_1$ (465.161 cm^{-1}) band of nitrous oxide. J Quant Spectrosc Radiat Transfer 1993;50:591-4.
28. Rachet F, Margottin-Maclou M, El Azizi M, Henry A, Valentin A. Linestrength measurements for the 3000-0200, 1001-0110, and 1310-0000 transitions of $^{14}N_2{}^{16}O$ (2600-3100 cm^{-1}). J Mol Spectrosc 1994;166:79-87.
29. Rachet F, Margottin-Maclou M, El Azizi M, Henry A, Valentin A. Linestrength measurements for N_2O around 4 μm: $\Pi \leftarrow \Sigma$, $\Pi \leftarrow \Pi$, $\Sigma \leftarrow \Pi$, and $\Delta \leftarrow \Pi$ transitions in $^{14}N_2{}^{16}O$ (2400-2850 cm^{-1}). J Mol Spectrosc 1994;164:196-209.
30. El Azizi M, Rachet F, Henry A, Margottin-Maclou M, Valentin A. Linestrength measurements for N_2O around 4 μm: $\Sigma \leftarrow \Sigma$ transitions in four isotopic species (2400-2600 cm^{-1}). J Mol Spectrosc 1994;164:180-95.
31. Chance K, Jucks KW, Johnson DG, Traub WA. The Smithsonian astrophysical observatory database SAO92. J Quant Spectrosc Radiat Transfer 1994;52:447-57.
32. Johns JWC, Lu Z, Weber M, Sirota JM, Reuter DC. Absolute intensities in the v_2 fundamental of N_2O at 17 μm. J Mol Spectrosc 1996;177:203-10.
33. Weber M, Sirota JM, Reuter DC. *l*-Resonance intensity effects and pressure broadening of N_2O at 17 μm. J Mol Spectrosc 1996;177:211-20.
34. Regalia L, Thomas X, Hamdouni A, Barbe A. Intensities of N_2O measurements in the 4 and 3 μm region using Fourier transform spectrometer. J Quant Spectrosc Radiat Transfer 1997;57:435-44.
35. Toth RA. Line positions and strengths of N_2O between 3515 and 7800 cm^{-1}. J Mol Spectrosc 1999;197:158-187.
36. Claveau C. LPMA, private communication (2000)
37. Daumont L, Vander Auwera J, Teffo JL, Perevalov VI, Tashkun SA. Line intensity measurements in $^{14}N_2{}^{16}O$ and their treatment using the effective dipole moment approach. I. The 4300- to 5200- cm^{-1} region. J Mol Spectrosc 2001;208:281-91.
38. Fukabori M, Aoki T, Watanabe T. Line intensities, N_2- and O_2- broadened half-widths in the v_1+v_3 band of $^{14}N_2{}^{16}O$ at room temperature. Atmos Ocean Optics 2003;16:217-22.
39. Parkes AM, Linsley AR, Orr-Ewing AJ. Absorption cross-sections and pressure broadening of rotational lines in the $3v_3$ band of N_2O determined by diode laser cavity ring-down spectroscopy. Chem Phys Lett 2003;377:439–44.
40. Nemtchinov V, Sun C, Varanasi P. Measurements of line intensities and line widths in the v_3-fundamental band of nitrous oxide at atmospheric temperatures. J Quant Spectrosc Radiat Transfer 2004;83:267-84.
41. Fukabori M, Aoki T, Watanabe T, Measurements of the line strengths, N2-, and O2-broadened half-widths in the 2ν2 +ν3 band of 14N216O at room temperatureJ Spectrosc Soc Japan 2004;53:80-6 doi 10.5111/bunkou.53.69
42. Wang L, Perevalov VI, Tashkun SA, Gao B, Hao LY, Hu SM. Fourier transform spectroscopy of N_2O weak overtone transitions in the 1–2 μm region. J Mol Spectrosc 2006;237:129-36.
43. Daumont L, Vander Auwera J, Teffo JL, Perevalov VI, Tashkun SA. Line intensity measurements in $^{14}N_2{}^{16}O$ and their treatment using the effective dipole moment approach. II. The 5400–11000 cm^{-1} region. J Quant Spectrosc Radiat Transfer 2007;104:342-56.

44. Grossel A, Zéninari V, Parvitte B, Joly L, Courtois D, Durry G. Quantum cascade laser spectroscopy of N_2O in the 7.9 μm region for the in situ monitoring of the atmosphere. J Quant Spectrosc Radiat Transfer 2008;109:1845-55.
45. Aenchbacher W, Naftaly M, Dudley R. Line strengths and self-broadening of pure rotational lines of nitrous oxide measured by terahertz time-domain spectroscopy. J Opt Soc Am B 2010;27:1717-21.
46. Milloud R, Perevalov VI, Tashkun SA, Campargue A. Rotational analysis of $6v_3$ and $6v_3+v_2-v_2$ bands of $^{14}N_2{}^{16}O$ from ICLAS spectra between 12,760 and 12,900 cm^{-1}. J Quant Spectrosc Radiat Transfer 2011;112:553-7.
47. Karlovets EV, Lu Y, Mondelain D, Kassi S, Campargue A, Tashkun SA, Perevalov VI. High sensitivity CW-Cavity Ring Down Spectroscopy of N_2O between 6950 and 7653cm^{-1} (1.44–1.31 μm): II. Line intensities. J Quant Spectrosc Radiat Transfer 2013;117:81-7.
48. Karlovets EV, Campargue A, Kassi S, Perevalov VI, Tashkun SA. High sensitivity Cavity Ring Down Spectroscopy of N_2O near 1.22 μm: (I) Rovibrational assignments and band-by-band analysis. J Quant Spectrosc Radiat Transfer 2016;169:36-48.
49. Bertin T, Mondelain D, Karlovets E, Kassi S, Perevalov V, Campargue A. High sensitivity cavity ring down spectroscopy of N_2O near 1.74 μm. J Quant Spectrosc Radiat Transfer 2019;229:40-9.
50. Odintsova TA, Fasci E, Gravina S, Gianfrani L, Castrillo A. Optical feedback laser absorption spectroscopy of N_2O at 2 μm. J Quant Spectrosc Radiat Transfer 2020;254:107190.
51. Karlovets EV, Kassi S, Tashkun SA, Campargue A. The absorption spectrum of nitrous oxide between 8325 and 8622 cm^{-1}. J Quant Spectrosc Radiat Transfer 2021;262:107508.
52. Adkins EM, Long DA, Fleisher AJ, Hodges JT. Near-infrared cavity ring-down spectroscopy measurements of nitrous oxide in the (4200) ← (0000) and (5000) ← (0000) bands. J Quant Spectrosc Radiat Transfer 2021;262:107527. doi:10.1016/j.jqsrt.2021.107527
53. Karlovets EV, Tashkun SA, Kassi S, Campargue A. An improved analysis of the N_2O absorption spectrum in the 1.18 μm window. J Quant Spectrosc Radiat Transfer 2022;278:108003. doi:10.1016/j.jqsrt.2021.108003.
54. Karlovets EV, Kassi S, Tashkun SA, Campargue A, The absorption spectrum of nitrous oxide between 7647 and 7918 cm^{-1} J Quant Spectrosc Radiat Transfer 2022;283:108199. doi 10.1016/j.jqsrt.2022.108199
55. Iwakuni K, Absolute frequency measurement of the $3v_1$ band of N_2O with comb-locked rapid scan spectroscopy using a multi-pass cell. J Mol Spectrosc 2022;384:111571. doi:10.1016/j.jms.2022.111571
56. Gamache RR, Vispoel B, Rey M, Nikitin A, Tyuterev Vl, Egorov O, Gordon IE Boudon V, Total internal partition sums for the HITRAN2020 database, J Quant Spectrosc Radiat Transfer 2021;271:107713. doi 10.1016/j.jqsrt.2021.107713
57. Transtrum MK, Machta BB, Brown KS, Daniels BC, Myers CR, Sethna JP. Perspective: sloppiness and emergent theories in physics, biology, and beyond. J Chem Phys 2015;143:010901. doi: 10.1063/1.4923066.
58. R.A. Toth, Jet Propulsion Laboratory, Linelist of N_2O parameters from 500 to 7500 cm^{-1}, private communication.
59. Bertseva E, Kachanov AA, Campargue A, Intracavity laser absorption spectroscopy of N 2 O with a vertical external cavity surface emitting laser. Chem Phys Lett 2002;351:18–26
60. Ding Y, Perevalov VI, Tashkun SA, Teffo JL, Hu S, Bertseva E, Campargue A, Weak overtone transitions of N_2O around 1.05 μm by ICLAS-VECSEL. J Mol Spectrosc 2003;220:80–6.
61. Bertseva E, Campargue A, Perevalov VI, Tashkun SA. New observations of weak overtone transitions of N_2O by ICLAS-VeCSEL near 1.07 μm. J Mol Spectrosc 2004;226:196–200.
62. Lu Y, Mondelain D, Liu AW, Perevalov VI, Kassi S, Campargue A, High sensitivity CW-Cavity Ring Down Spectroscopy of N_2O between 6950 and 7653 cm^{-1} (1.44-1.31 μm): I. Line positions. J Quant Spectrosc Radiat Transfer 2012;113:749–62.
63. Tashkun SA, Perevalov VI, Gamache RR, Lamouroux J, CDSD-296, high-resolution carbon dioxide spectroscopic databank: An update, J Quant Spectrosc Radiat Transfer 2019;228:124-31.

Declaration of Competing Interest

The authors declare that they have no known competing financial interests or personal relationships that could have appeared to influence the work reported in this paper.

CRediT authorship contribution statement

S.A. Tashkun: Investigation, Writing –review & editing.

A. Campargue: Writing –review & editing.

Supplementary materials

Supplementary material associated with this article can be found, in the online version, at doi